HHS Public Access

Author manuscript

Magn Reson Med. Author manuscript; available in PMC 2022 February 24.

Published in final edited form as:

Magn Reson Med. 2022 January ; 87(1): 541–550. doi:10.1002/mrm.28977.

Minimal Artifact Actively Shimmed Metallic Needles in MRI

Saikat Sengupta[a,b], **Xinqiang Yan**[a,b], **Tamarya L. Hoyt**[b], **Gary Drake**[a], **Anthony Gunderman**[c], **Yue Chen**[c]

[a.]Vanderbilt University Institute of Imaging Science, Vanderbilt University Medical Center, Nashville, TN, 37235, USA

[b.]Department of Radiology and Radiological Sciences, Vanderbilt University Medical Center, Nashville, TN, 37235, USA

[c.]Department of Mechanical Engineering, University of Arkansas, Fayetteville, AR, 72701, USA

Abstract

Purpose: Signal voids caused by metallic needles pose visualization and monitoring challenges in many MRI applications. In this work we explore a solution to this problem in the form of an active shim insert that fits inside a needle and corrects the field disturbance (ΔB_0) caused by the needle outside of it.

Methods: The ΔB_0 induced by a 4mm OD Titanium needle at 3 Tesla is modeled and a 2-coil orthogonal shim set is designed and fabricated to shim the ΔB_0. Signal recovery around the needle is assessed in multiple orientations in a water phantom with four different pulse sequences. Phase stability around the needle is assessed in an *ex-vivo* porcine tissue dynamic gradient echo experiment with and without shimming. Additionally, heating of the shim insert is assessed under 8 minutes of continuous operation with 1A current and concurrent imaging.

Results: An average recovery of ~63% of lost signal around the needle across orientations is shown with active shimming with a maximum current of 1.172 A. Signal recovery and correction of the underlying ΔB_0 is shown to be independent of imaging sequence. Needle-induced phase gradients outside the perceptible signal void are also minimized with active shimming. Temperature rise of up to 0.9° Celsius is noted over 8 minutes of continuous 1A active shimming operation.

Conclusion: A sequence independent method for minimization of metallic needle induced signal loss using an active shim insert is presented. The method has potential benefits in a range of qualitative and quantitative interventional MRI applications.

Keywords

Interventional MRI; Metallic Needles; Active Shimming; Shim coils; Field inhomogeneity

Corresponding Author: Saikat Sengupta, Ph.D., Vanderbilt University Institute of Imaging Science, 1161 21st Avenue South, Medical Center North, AA-1105, Nashville, TN 37232-2310, Phone No: 1(615) 3430471, Fax: 1(615) 322-0734, saikat.sengupta@vumc.org.

Conflict of interest statement

The topic of this work has been submitted for a United States patent application

INTRODUCTION

Susceptibility artifacts caused by metallic needles present challenges in several MRI applications[1-5]. Magnetic susceptibility differences between metal and tissue induce significant field perturbations (ΔB_0) and cause intravoxel signal loss, distortions and signal pileups around the needle[1-5]. In MR-guided biopsies, artifacts obscure targets, vital anatomies, landmarks and the actual device position[6-16]. In MR-guided brachytherapy, they cause inaccuracies in treatment planning, pellet placement and dose calculation[17-19]. In MR-guided radiofrequency[20], microwave[21] and cryo-ablations[22-24], artifacts hinder qualitative and quantitative phase-based monitoring of therapy[25]. Applications of simultaneous electrophysiology with MRI are also limited by artifacts around the metal electrodes that prevent accurate localization of the electrodes and acquisition of MR signals from their immediate vicinity[26,27].

Needle artifacts have been characterized in several studies in the past [4,28,29]. Glass and plastic needles with lesser artifacts have been presented, but they are prone to bending and breaking[5]. One proposed solution was to coat paramagnetic titanium with diamagnetic bismuth to produce a composite material needle[30]. Carbon fiber needles have also been shown to produce low susceptibility artifacts[31,32]. Imaging techniques designed to better image around metal implants such as MAVRIC[33-36], SEMAC[37], VAT[3] or MARS[3,38-40] may also be applied to image around needles. However, a majority of these sequences are time consuming and SAR intensive and not ideal for applications where rapid and repetitive imaging is important for tracking of instruments, targeting of moving organs or continuous quantitative monitoring. Therefore, a compensation method that tackles the issue at the source, i.e., the needle, could be significant in enabling imaging with a variety of sequences, at high frame rates and higher fields.

The goal of this work is to explore a solution to this problem in the form of a multicoil active shim insert that is designed to fit inside the metallic needle and produce a field that corrects the ΔB_0 outside of it. In our earlier work, we presented modelling studies to demonstrate the correction of the ΔB_0 around a 10-gauge titanium needle[41]. In this paper, we present the fabrication of a shim insert and correction of the signal void artifact around a titanium needle at 3 Tesla. Signal recovery and correction of the underlying ΔB0 across different imaging sequences and needle orientations is demonstrated. Phase stability around the needle is also assessed in a dynamic gradient echo experiment. The benefits, design challenges and safety concerns of actively shimmed needles are discussed.

METHODS

Simulations

The needle induced field, shim coil paths, shim coil fields and field shimming were first simulated to estimate the expected corrections and required shim currents. The scanner's coordinate frame was defined as X_M : up-down, Y_M : left-right and Z_M : in and out of the bore (also the scanner's B_0 axis). Rotations about the axes were defined in the left-handed system and denoted by three values in degrees. Without any rotations (0,0,0-degree), the needle was oriented vertically with the beveled tip pointing down along $-X_M$ (Figure 1a). We

have reported shimming simulations in detail in our earlier work[41], and a similar procedure was followed here. Shim coils were simulated for a 4/3 mm OD/ID, hollow Titanium needle with a 30° single-sided bevel at the tip (Volume Susceptibility: $\chi = 182*10^{-}$)[42] with water inside and around it ($\chi = -9.05*10^{-6}$)[42] at 3 Tesla. 18 candidate shim coil sets comprising of 2 orthogonal coils, CN0 and CN90, were defined to fit inside the needle. For all coils, a radial clearance of 0.25 mm from the inner radius of the needle was included to allow space for insulation. Also, a separation of 0.4 mm (one wire diameter) along the needle's length was included between CN0 and CN90 to minimize conductor overlap. Shimming performance was evaluated by fitting the needle induced fields with each of the 18 coil pair fields for four needle orientations: (0,0,0), (90,0,0), (0,−90,0) and (90,−90,0) degrees with a ±1.5 A constrained least squares fit in Matlab and the combination with the lowest summed shimmed to unshimmed ΔB_0 ratio over all four orientations was selected as the final tip path[41].

Based on these simulations, a ½ turn loop angled at the bevel angle 6 mm from the tip was chosen as the best CN90 design in combination with a split 2 path CN0 loop placed 4.2 mm from the tip (Figure 1a). All experiments were performed with this design.

Hardware

Needle and Shim Insert Fabrication—A needle was fabricated from a 15 cm long 4/3 mm OD/ID hollow titanium tube with a 30° single-sided bevel on one tip. For mounting the shim coils, a 2.5 mm diameter, 16 cm former with a bevel was designed in Solidworks (Dassault Systemes, MA, USA). Orthogonal, 0.5 mm diameter wire slots were incorporated in the former according to the simulated CN0 and CN90 wire paths. For the CN0 coil, the slot was widened to a width of 1.0 mm to hold two 0.4 mm conductors instead of one. This design modification eased the fabrication of the split in the CN0 coil. Each leg of the coil therefore carried half of the supplied CN0 current. (Figure 1b).

The insert was 3D printed (ProJet 3500 HD Max, 3D Systems Inc, USA) and the wire slots were cleaned and cleared with acetone. 26-gauge enameled copper wire was placed into the slots by hand, and a single layer of kapton tape was wrapped around the insert for insulation. The insert was then slid inside the needle and the bevels aligned with each other (Figure 1c). A holder with a compartment for shim wire connections was 3D printed (CR10 PLA printer, Creality 3D, China, Figure 1d) and the needle was tightened into a central bore hole in the holder. Inside the holder, the shim wires were connected to 20 feet long twisted cable that were guided through the holder handle. A pair of low profile 127 MHz RF chokes[48] were placed in line along each current path to minimize induced currents during RF transmit pulses.

Experiments

All experiments were performed on a Philips 3 Tesla Elition scanner with a 2-channel body RF transmit coil and a 16-channel head and neck receive coil (Philips Healthcare, Eindhoven, Netherlands). Two 15 cm diameter cylindrical phantoms with domes that allowed needle insertions at different angles were designed and printed using the PLA 3D printer (Figure 1e). The first phantom had insertion guide holes only in the dome and

was used for tap-water experiments. The second phantom had guide holes along the sides and a screw top and was used for an *ex-vivo* porcine tissue experiment. The shim coils were supplied by a 2-channel constant current power supply (KeySight E3631A, Keysight Technologies, CA, USA, 6V/±5A, 25V//±1A).

Shim Coil Heating Tests—Incorporating current carrying conductors inside a needle introduces the possibility of added temperature rise due to resistive and RF induced heating[49]. To assess this, we performed tests of needle and shim coil heating according the ASTM-F2182 standard[50]. The setup of the heating experiment is shown in Supporting Information Figure S3. A 65 x 42 x 9 cm^3 polyacrylic acid - NaCl phantom with needle holders was fabricated for the experiments. The average electrical conductivity of the phantom measured over four different locations was 0.467 S/m. Temperature measurements were performed with two fiber optic temperature probes (Luxtron m3300, LumaSense, California, USA), one placed at the tip of needle and the second placed on the body, 5 cm from the tip. A first set of tests was performed with the shim insert inside the needle in two different orientations, perpendicular to B_0 (0,0,0 degrees) and parallel to B_0 (0,−90,0 degrees), with the needle located 15 cm to the right of isocenter. An off-center position was selected because RF induced heating is known to be higher in off-center positions compared to the center of the bore[49]. The needle was immersed in the phantom for all experiments. Temperature was recorded every 10s for 8 mins of 3D FSE and continuous 2D SSFP imaging (parameters in Supporting Information Table S4-C). Tests were conducted under three conditions: No current in the shim coils, 1A in CN0 and 1A in CN90. In all experiments, a baseline period of 1 minute preceded the concurrent start of imaging and current supply. In a second set of tests, the measurements were repeated without the needle, with probes placed directly on the shim coils; probe 1 on CN0 tip and probe 2 on CN90, 5 cm from the tip. Two sets of reference measurements were also conducted. In the first, the temperature probes were placed in the center and off-center positions in the scanner without the needle or shim insert, and imaging was performed with the same sequences. The second reference measurement was performed outside the scanner. Probes were placed directly on the shim insert immersed vertically in the center of the phantom and measurements were made with 1A current supplied to the two shim coils individually. In all experiments, the temperature was allowed to return to completely to baseline before commencing the subsequent run. The final temperature rise was estimated by subtracting the average one-minute baseline temperature from the temperature at the end of scanning.

Needle Shimming Experiments—Prior to experiments that demonstrated needle shimming, a validation experiment was conducted to ensure that the shim coils were producing fields that matched theoretical predictions. Details of this experiment are provided in Supporting Information Text and Supporting Information Figure S1. After validating that the shim coil fields matched theoretical fields, full needle shimming experiments were conducted using Phantom 1 filled with tap water. The experiment was conducted with the phantom in two positions, once at the center of the bore, and once 13 cm to the left of the central plane to mimic off-center needle positions commonly encountered in MR guided applications (Figure 1f). First, the currents necessary to shim the needle at four different orientations: i) 0,0,0 ii) 90,0,0 iii) 0,18,30 and iv) 20, −30,0 degrees were

simulated. The needle containing the insert was then inserted into the water phantom through the guide holes in these four orientations and imaging was performed with 3D GRE with fieldmapping, 3D FSE, 2D single slice balanced SSFP and single slice multishot EPI sequences (Supporting Information Table S4-A). In all orientations, the imaging stack was oriented along the plane of the needle bevel. For each orientation, images were acquired without and with the precalculated shim currents supplied to the two coils.

The objective of a second needle shim experiment was to assess spatial and temporal phase variations around a needle with shimming. Phase stability around interventional probes is important in therapeutic applications for treatment monitoring using proton resonance shift methods. We assessed this in two orientations, one with the needle perpendicular to $\boldsymbol{B_0}$ (0,0,90 degrees) and one with the needle parallel to $\boldsymbol{B_0}$ (0, −90,0 degrees). Shim currents needed for both orientations were first estimated by simulations. An *ex-vivo* porcine muscle sample was placed inside phantom 2. The needle was inserted into the sample in the two orientations and continuous 3D GRE was performed for ~9 minutes and phase images were collected with and without shimming (parameters in Supporting Information Table S4-B). 1D phase unwrapping was performed in the time and in-plane dimensions using a least squares FFT algorithm in Matlab[51]. To evaluate phase stability, voxelwise standard deviations over time of the image phase were estimated from the unwrapped phase images.

RESULTS

Needle Shimming Experiments

Simulations predicted the need for i) 1.17A, 0 A ii) 0A, −1.15 A ii) 0.97 A, 0 A and iv) 0.819 A, −0.29 A in CN0 and CN90 coils for the four needle orientations in the first experiment. Figure 2 shows images from the 3D GRE acquisitions along with the acquired fieldmaps. Significant recovery of the lost signal around the needle is evident in all four orientations with shimming using the pre-determined shim currents. The estimated volume of the signal void reduced from 8097, 8047, 3324 and 5072 mm^3 without shimming to 2510, 2816, 1428, 1995 mm^3 with shimming respectively in the four orientations. This represented recovery of 69.0%, 64.9%, 57.1% and 60.6% of the lost signal with an average of −63% over all orientations. The true fraction of the recovered signal is in-fact higher since the volume of the needle itself could not be accurately estimated and accounted for. The fieldmaps show the correction of the underlying ΔB_0. Without shimming, there is significant fieldwrapping around the needle due to extremely high ΔB_0, which is almost completely eliminated with shimming. Note also that there is no field information in the areas close to the needle without shimming. Furthermore there is a notable ΔB_0 gradient around the needle even in the areas with apparent high signal before shimming, which is removed by shimming. Similar shimming performance was obtained with the phantom in the off-center position (Supporting Information Figure S2).

Figure 3 shows balanced SSFP, 3D FSE and multishot EPI images without and with shimming. Consistent recovery of signal is evident in all sequences. Balanced SSFP images show significantly reduced off-resonance banding around the already minimized signal void due to the reduced ΔB_0 gradients around the needle. In FSE, the voids (caused by slice and in-plane distortions) are minimized to the point of approaching the true needle width.

Finally, multishot EPI images also show reduced voids and although not assessed here, it is reasonable to expect significantly reduced image distortions with active shimming in the areas surrounding the needle void.

Figure 4 shows GRE images, phase maps and phase stability maps from the *ex-vivo* porcine muscle experiment. Active shimming was effective in reducing the signal void when the needle was perpendicular to $\boldsymbol{B_0}$ (0,0,90 degrees). When the needle was parallel to $\boldsymbol{B_0}$ (0, −90,0 degrees), shimming did not have noticeable impact on the signal void. This was expected from simulations based on the chosen coil structure and has been discussed in detail in our earlier simulation work[47]. The phase precision maps did not show significant differences between the shimmed and unshimmed cases, apart from the much larger uncorrected void in the latter. However, a much steeper phase gradient around the void was noted in the unshimmed needle. Reduction of these high background phase gradients could potentially make *in-vivo* phase-difference-based measurements much more robust to effects of motion and respiration.

Shim Coil Heating Tests

The results of temperature testing of the shim insert with and without the needle are shown in Table 1. With the needle in place, heating in the range of 0.3-2.79° Celsius was observed. Higher heating was observed at the tip of the needle (probe 1) than 5 cm away from the tip (probe 2). Also, higher heating was observed when the needle was parallel to B_0 compared to the perpendicular position. Higher heating was also noted with 3D FSE compared to SSFP imaging. Importantly, higher heating in the range of 0.1-0.9° Celsius was noted with 1A shim currents turned on, indicating at least some direct resistive heating of the shim coils. When the temperature probes were placed directly on the shim coils, heating in the range of 0.36-1.74° Celsius was observed without any currents. Also, higher heating was noted with 3D FSE than SSFP. Both of these results indicated transmit RF induced temperature rise of the conductive shim wires. Additionally, introduction of 1A currents again led to higher heating in the range of 0.2-0.9° Celsius.

DISCUSSION AND CONCLUSION

In this paper, we have presented the first experimental demonstration of an actively shimmed metallic needle for use in an MRI scanner. In the sections below, we discuss some of the possibilities, challenges and potential solutions to translating this technique.

The fields generated by the shim insert matched the simulated fields well in general. Slight deviations could be attributed to inaccuracies in manual coil fabrication, which may be alleviated with mechanized fabrication processes in the future. While we employed a titanium needle here, shimming is expected to work for stainless steel needles as well, albeit with higher currents. Simulations predict that full, unconstrained shimming of a 14-gauge stainless steel needle at 3 Tesla would require ~3.3 A compared to ~380 mA for titanium. A potential benefit of shimmed needles is the ability to control artifact size by adjusting the shim currents, which might aid in needle visualization. Such technology based on DC currents has been explored earlier for visualization and tracking of catheters[52-54]. For real

time tracking of needle orientation and adaptive needle shimming, optical or RF based needle tracking techniques can be integrated[55,56].

One design challenge in this technique is the space inside a needle and whether shim conductors might be incorporated with minimal compromise on the core function of the device. For probes with working central channels, shim inserts with flexible printed coils mounted on thin wall hollow tubes could be conceived that leave the central working channel open[57]. Alternatively, shim inserts that are retractable can be designed. The shim insert in this work did not exhibit noticeable torque when operated in the scanner's bore. For larger diameter inserts or for inserts requiring more current, torque balanced designs with reversed directions of the shim coils in the upper half of the needle could be conceived.

The biggest challenge in this technology is ensuring safety. There exists a hazard of electric shock due to current leakage from the shim coil to the needle metal and the body. To address this, the insert can be designed such that the shim wires are fully embedded in an insulating substrate, so that the shim coils never come in contact with the metal. Also, a shunt resistor-based detection circuit can be integrated to detect current leaks in the metal and switch off the circuit. Additionally, a current stepping protocol could be followed in which the current is stepped to an initial test level calibrated to trip the circuit in case of a leak, prior to ramping to the required level for shimming. A second safety concern is the possibility of arcing between the shim coils. Given the relatively low voltages required to drive the shim currents, (the coils here required 2.2 V), and the high dielectric strengths of 3D printed resin in the range of 20-40 KV/mm[58], arcing is highly unlikely. Additionally, MRI compatible lithium-ion batteries could potentially be used to power the shim coils and eliminate the cabling from the needle to the power supply, which would further reduce the voltage demand and risk of arcing. A third issue that has been explored in this work is shim insert heating. In our experiments, we recorded up to 0.9° Celsius of additional temperature rise due to the shim coils using 1A current supplied over 8 minutes via fairly large 26-gauge shim wires. In higher gauge wires for finer needles, resistive heating is expected to be higher. Given the possible variations in device and shim coil geometries, it would be therefore important to assess heating in a device per device basis. In summary, some important safety concerns do exist with this technique, and more work is needed to fully evaluate these risks and design protection strategies. Nevertheless, the method could find applications in the near term in phantom and ex-vivo studies for the development of interventional devices, robots and MRI sequences and in-vivo animal studies where the risk criteria might be different.

Supplementary Material

Refer to Web version on PubMed Central for supplementary material.

ACKNOWLEDGEMENTS

This work was supported by funding from NIBIB R21EB025258. The authors would like to thank William A. Grissom, John C. Gore, Robert Webster and Megan Poorman for advice on the topic, helpful discussions.

REFERENCE

1. Weiss CR, Nour SG, Lewin JS. MR-guided biopsy: a review of current techniques and applications. J Magn Reson Imaging. 2008;27(2):311–25. doi: 10.1002/jmri.21270. PMID: 18219685 [PubMed: 18219685]
2. Nour SG, Lewin JS. Percutaneous biopsy from blinded to MR guided: an update on current techniques and applications. Magn Reson Imaging Clin N Am. 2005;13(3):441–64. PMID: 16084412 DOI: 10.1016/j.mric.2005.04.009 [PubMed: 16084412]
3. Butts K, Pauly JM, Daniel BL, Kee S, Norbash AM. Management of biopsy needle artifacts: techniques for RF-refocused MRI. J Magn Reson Imaging. 1999 ;9(4):586–95. PMID: 10232519 [PubMed: 10232519]
4. Müller-Bierl B, Graf H, Lauer U, Steidle G, Schick F. Numerical modeling of needle tip artifacts in MR gradient echo imaging. Med Phys. 2004;31(3): 579–87 PMID: 15070257 [PubMed: 15070257]
5. Penzkofer T, Peykan N, Schmidt K, Krombach G, Kuhl CK How MRI compatible is "MRI compatible"? A systematic comparison of artifacts caused by biopsy needles at 3.0 and 1.5 T. Cardiovasc Intervent Radiol. 2013;36(6):1646–57. PMID: 23580119 DOI: 10.1007/s00270-013-0616-0 [PubMed: 23580119]
6. Kuhl CK, Morakkabati N, Leutner CC, Schmiedel A, Wardelmann E, Schild HH. MR imaging--guided large-core (14-gauge) needle biopsy of small lesions visible at breast MR imaging alone. Radiology. 2001 ;220(1):31–9. PMID: 11425969 DOI: 10.1148/radiology.220.1.r01jl0731 [PubMed: 11425969]
7. Peters NH, Meeuwis C, Bakker CJ, Mali WP, Fernandez-Gallardo AM, van Hillegersberg R, Schipper ME, van den Bosch MA. Feasibility of MRI-guided large-core-needle biopsy of suspiscious breast lesions at 3 T. Eur Radiol. 2009;19(7):1639–44. PMID: 19214520 PMCID: PMC2691521 DOI: 10.1007/s00330-009-1310-0 [PubMed: 19214520]
8. Dogan BE, Le-Petross CH, Stafford JR, Atkinson N, Whitman GJ. MRI-guided vacuum-assisted breast biopsy performed at 3 T with a 9-gauge needle: preliminary experience. AJR Am J Roentgenol. 2012;199(5): W651–3. doi: 10.2214/AJR.11.8055. [PubMed: 23096211]
9. Plantade R, Thomassin-Naggara I MRI vacuum-assisted breast biopsies. Diagn Interv Imaging. 2014;95(9):779–801. PMID: 24636589 DOI: 10.1016/j.diii.2013.12.023 [PubMed: 24636589]
10. Daniel BL, Freeman LJ, Pyzoha JM, McCoy TD, Birdwell RL, Bouley DM, Movius B, Hibner JA. An MRI-compatible semiautomated vacuum-assisted breast biopsy system: initial feasibility study. J Magn Reson Imaging. 2005 ;21(5):637–44. PMID: 15834914 DOI: 10.1002/jmri.20302 [PubMed: 15834914]
11. Dianat SS, Carter HB, Macura KJ. Magnetic Resonance-Guided Prostate Biopsy. Magn Reson Imaging Clin N Am. 2015 ;23(4):621–31 PMID: 26499279 DOI: 10.1016/j.mric.2015.05.005 [PubMed: 26499279]
12. Song SE, Cho NB, Iordachita II, Guion P, Fichtinger G, Kaushal A, Camphausen K, Whitcomb LL. Biopsy needle artifact localization in MRI-guided robotic transrectal prostate intervention. IEEE Trans Biomed Eng. 2012;59(7):1902–11. PMID: 22481805 PMCID: PMC3675798 DOI: 10.1109/TBME.2012.2192118 [PubMed: 22481805]
13. Liu H, Hall WA, Martin AJ, Truwit CL. Biopsy needle tip artifact in MR-guided neurosurgery. J Magn Reson Imaging. 2001;13(1):16–22. PMID: 11169798 [PubMed: 11169798]
14. Thomas C, Springer F, Rothke M, Rempp H, Clasen S, Fritz J, Claussen CD, Pereira PL. In vitro assessment of needle artifacts with an interactive three-dimensional MR fluoroscopy system. J Vasc Interv Radiol. 2010 ;21(3):375–80. PMID: 20171560 DOI: 10.1016/j.jvir.2009.11.012 [PubMed: 20171560]
15. Liu M, Sequeiros RB, Xu Y, He X, Zhu T, Li L, Lü Y, Huang J, Li C.MRI-guided percutaneous transpedicular biopsy of thoracic and lumbar spine using a 0.23t scanner with optical instrument tracking. J Magn Reson Imaging. 2015 ;42(6):1740–6. PMID: 25946392 DOI: 10.1002/jmri.24924 [PubMed: 25946392]
16. Kühn JP, Langner S, Hegenscheid K, Evert M, Kickhefel A, Hosten N, Puls R. Magnetic resonance-guided upper abdominal biopsies in a high-field wide-bore 3-T MRI system: feasibility,

handling, and needle artefacts. Eur Radiol. 2010 ;20(10):2414–21. PMID: 20503050 DOI: 10.1007/s00330-010-1809-4 [PubMed: 20503050]

17. Frank SJ, Stafford RJ, Bankson JA, Li C, Swanson DA, Kudchadker RJ, Martirosyan KS. A novel MRI marker for prostate brachytherapy. Int J Radiat Oncol Biol Phys. 2008 ;71(1):5–8. PMID: 18406882 DOI: 10.1016/j.ijrobp.2008.01.028 [PubMed: 18406882]
18. Hata N, Blumenfeld P, diMaio S et al., Needle placement accuracy in MRI_guided prostate biopsy of prostate cancer. Proceedings of the 14th Annual Meeting of ISMRM, Seattle, USA, 2006, pp 1440
19. Wachowicz K, Thomas SD, Fallone BG. Characterization of the susceptibility artifact around a prostate brachytherapy seed in MRI. Med Phys. 2006;33(12):4459–67. PMID: 17278797 DOI: 10.1118/1.2364052 [PubMed: 17278797]
20. Clasen S, Pereira PL. Magnetic resonance guidance for radiofrequency ablation of liver tumors. J Magn Reson Imaging. 2008;27(2):421–33. doi: 10.1002/jmri.21264.. PMID: 18219677 DOI: 10.1002/jmri.21264 [PubMed: 18219677]
21. Hoffmann R, Rempp H, Eibofner F, Keßler DE, Blumenstock G, Weiß J, Pereira PL, Nikolaou K, Clasen S. In vitro artefact assessment of a new MR-compatible microwave antenna and a standard MR-compatible radiofrequency ablation electrode for tumour ablation. Eur Radiol. 2016 ;26(3):771–9. doi: 10.1007/s00330-015-3891-0. Epub 2015 Jul 2. [PubMed: 26134999]
22. Liu X, Tuncali K, Wells WM, Zientara GP. Automatic probe artifact detection in MRI-guided cryoablation. Proceedings of the 2013 SPIE, Medical Imaging: Image-Guided Procedures, Robotic Interventions, and Modeling Conference pp 8671 DOI: 10.1117/12.2008530.
23. Daniel BL, Butts K. The use of view angle tilting to reduce distortions in magnetic resonance imaging of cryosurgery. Magn Reson Imaging. 2000;18(3):281–6. PMID: 10745137 [PubMed: 10745137]
24. Kickhefel A, Weiss C, Roland J, Gross P, Schick F, Salomir R. Correction of susceptibility-induced GRE phase shift for accurate PRFS thermometry proximal to cryoablation iceball. MAGMA. 2012;25(1):23–31. PMID: 21898135 DOI: 10.1007/s10334-011-0277-4 [PubMed: 21898135]
25. Rieke V, Vigen KK, Sommer G, Daniel BL, Pauly JM, Butts K. Referenceless PRF shift thermometry. Magn Reson Med. 2004;51(6):1223–31. PMID: 15170843 DOI: 10.1002/mrm.20090 [PubMed: 15170843]
26. Van Den Berge N, Vanhove C, Descamps B, Dauwe I, van Mierlo P, Vonck K, Keereman V, Raedt R, Boon P, Van Holen R. Functional MRI during Hippocampal Deep Brain Stimulation in the Healthy Rat Brain. PLoS One. 2015 Jul 20;10(7):e0133245. [PubMed: 26193653]
27. In MH, Cho S, Shu Y, Min HK, Bernstein MA, Speck O, Lee KH, Jo HJ. Correction of metal-induced susceptibility artifacts for functional MRI during deep brain stimulation. Neuroimage. 2017 Sep; 158:26–36.. [PubMed: 28666879]
28. Glowinski A, Adam G, Bücker A, van Vaals J, Günther RW. A perspective on needle artifacts in MRI: an electromagnetic model for experimentally separating susceptibility effects. IEEE Trans Med Imaging. 2000 Dec;19(12):1248–52. PMID: 11212373 DOI: 10.1109/42.897817 [PubMed: 11212373]
29. Park YL, Elayaperumal S, Daniel B, Ryu SC, Shin M, Savall J, Black RJ, Moslehi B, Cutkosky MR. Real-Time Estimation of 3-D Needle Shape and Deflection for MRI-Guided Interventions. IEEE ASME Trans Mechatron. 2010;15(6):906–915. PMID: 26405428 PMCID: PMC4577522 DOI: 10.1109/TMECH.2010.2080360 [PubMed: 26405428]
30. Müller-Bierl B, Graf H, Steidle G, Schick F. Compensation of magnetic field distortions from paramagnetic instruments by added diamagnetic material: measurements and numerical simulations. Med Phys. 2005;32(1):76–84. PMID: 15719957 DOI: 10.1118/1.1828674 [PubMed: 15719957]
31. Reichenbach JR, Wurdinger S, Pfleiderer SO, Kaiser WA. Comparison of artifacts produced from carbon fiber and titanium alloy needles at 1.5 T MR imaging. J Magn Reson Imaging. 2000 Jan;11(1):69–74. PMID: 10676624. [PubMed: 10676624]
32. Thomas C, Springer F, Röthke M, Rempp H, Clasen S, Fritz J, Claussen CD, Pereira PL. In vitro assessment of needle artifacts with an interactive three-dimensional MR fluoroscopy system. J

Vasc Interv Radiol. 2010 Mar;21(3):375–80. doi: 10.1016/j.jvir.2009.11.012. PMID: 20171560. [PubMed: 20171560]

33. Koch KM, Lorbiecki JE, Hinks RS, King KF. A multispectral three-dimensional acquisition technique for imaging near metal implants. Magn Reson Med. 2009 ;61(2):381–90. PMID: 19165901 DOI: 10.1002/mrm.21856 [PubMed: 19165901]
34. Koch KM, Brau AC, Chen W, Gold GE, Hargreaves BA, Koff M, McKinnon GC, Potter HG, King KF. Imaging near metal with a MAVRIC-SEMAC hybrid. Magn Reson Med. 2011 ;65(1):71–82. PMID: 20981709 DOI: 10.1002/mrm.22523 [PubMed: 20981709]
35. Weber H, Taviani V, Yoon D, Ghanouni P, Pauly KB, Hargreaves BA. MR thermometry near metallic devices using multispectral imaging. Magn Reson Med. 2017 Mar;77(3):1162–1169. doi: 10.1002/mrm.26203. Epub 2016 Mar 16. PMID: 26991803; PMCID: PMC5532173 [PubMed: 26991803]
36. Weber H, Hargreaves BA, Daniel BL. Artifact-reduced imaging of biopsy needles with 2D multispectral imaging. Magn Reson Med. 2018 Aug;80(2):655–661. doi: 10.1002/mrm.27056. Epub 2017 Dec 29. PMID: 29285787; PMCID: PMC5910245. [PubMed: 29285787]
37. Lu W, Pauly KB, Gold GE, Pauly JM, Hargreaves BA. SEMAC: Slice Encoding for Metal Artifact Correction in MRI. Magn Reson Med. 2009 ;62(1):66–76. PMID: 19267347 PMCID: PMC2837371 DOI: 10.1002/mrm.21967 [PubMed: 19267347]
38. Olsen RV, Munk PL, Lee MJ, Janzen DL, MacKay AL, Xiang QS, Masri B. Metal artifact reduction sequence: early clinical applications. Radiographics. 2000;20(3):699–712. PMID: 10835123 DOI: 10.1148/radiographics.20.3.g00ma10699 [PubMed: 10835123]
39. Kolind SH, MacKay AL, Munk PL, Xiang QS. Quantitative evaluation of metal artifact reduction techniques. J Magn Reson Imaging. 2004;20(3):487–95. PMID: 15332257 [PubMed: 15332257]
40. Lewin JS, Duerk JL, Jain VR, Petersilge CA, Chao CP, Haaga JR. Needle localization in MR-guided biopsy and aspiration: effects of field strength, sequence design, and magnetic field orientation. AJR Am J Roentgenol. 1996;166(6):1337–45. PMID: 8633445 [PubMed: 8633445]
41. Sengupta S Modeling of active shimming of metallic needles for interventional MRI. Magn Reson Med. 2020 Nov;84(5):2858–2870. doi: 10.1002/mrm.28320. Epub 2020 Jun 29. PMID: 32597521; PMCID: PMC7396316. [PubMed: 32597521]
42. Schenck JF. The role of magnetic susceptibility in magnetic resonance imaging: MRI magnetic compatibility of the first and second kinds. Med Phys. 1996 ;23(6):815–50. [PubMed: 8798169]
43. Aitkenhead AH. https://www.mathworks.com/matlabcentral/fileexchange/27390-mesh-voxelisation. Published April 28, 2010. Updated February 12, 2013. Accessed October 23, 2018.
44. Salomir R, de Senneville BD, Moonen CT. A fast calculation method for magnetic field inhomogeneity due to an arbitrary distribution of bulk susceptibility. Concepts Magn. Reson, 2003, 19B: 26–34. doi:10.1002/cmr.b.10083
45. Marques JP, Bowtell R. Application of a Fourier-based method for rapid calculation of field inhomogeneity due to spatial variation of magnetic susceptibility. Concepts Magn. Reson, 2005, 25B: 65–78. doi:10.1002/cmr.b.20034
46. Ramm P, PhD Thesis, Universität Regensburg 2012. https://epub.uni-regensburg.de/20948/.
47. Masullo A https://www.mathworks.com/matlabcentral/fileexchange/42237-biot-savart-direct-integration-on-a-generic-curve. Published June 19, 2013. Accessed September 12, 2017.
48. Xia J, Sappo CR, Grissom WA, Yan X Low-profile AC/DC coils without RF Chokes Proceedings of the 28th Annual Meeting of ISMRM, Virtual Meeting, 2020, pp 1276
49. Khodarahmi I, Bonham LW, Weiss CR, Fritz J. Needle Heating During Interventional Magnetic Resonance Imaging at 1.5- and 3.0-T Field Strengths. Invest Radiol. 2020 Jun;55(6):396–404. doi: 10.1097/RLI.0000000000000649. PMID: 32369319. [PubMed: 32369319]
50. A American Society for Testing and Materials International. Standard Test Method for Measurement of Radiofrequency Induced Heating on or Near Passive Implants During Magnetic Resonance Imaging: ASTM Standard F2182-11a, 2002. West Conshohocken, PA: ASTM International; 2011
51. Pritt M, Shipman JS. Least-squares two-dimensional phase unwrapping using FFT's. IEEE Trans. Geosci. Remote. Sens 32 (1994): 706–708.

52. Glowinski A, Adam G, Bücker A, Neuerburg J, van Vaals JJ, Günther RW. Catheter visualization using locally induced, actively controlled field inhomogeneities. Magn Reson Med. 1997 Aug;38(2):253–8. [PubMed: 9256105]

53. Adam G, Glowinski A, Neuerburg J, Bücker A, van Vaals JJ, Günther RW. Visualization of MR-compatible catheters by electrically induced local field inhomogeneities: evaluation in vivo. J Magn Reson Imaging. 1998 Jan-Feb;8(1):209–13. [PubMed: 9500282]

54. Roberts TP, Hassenzahl WV, Hetts SW, Arenson RL. Remote control of catheter tip deflection: an opportunity for interventional MRI. Magn Reson Med. 2002 Dec;48(6):1091–5. [PubMed: 12465124]

55. Coutts GA, Gilderdale DJ, Chui M, Kasuboski L, DeSouza NM. Integrated and interactive position tracking and imaging of interventional tools and internal devices using small fiducial receiver coils. Magn Reson Med. 1998 Dec;40(6):908–13. [PubMed: 9840836]

56. Kägebein U, Godenschweger F, Armstrong BSR, Rose G, Wacker FK, Speck O, Hensen B. Percutaneous MR-guided interventions using an optical Moire Phase tracking system: Initial results.PLoS One. 2018 Oct 16;13(10): e0205394. [PubMed: 30325955]

57. Yildirim DK, Bruce C, Uzun D, Rogers T, O'Brien K, Ramasawmy R, Campbell-Washburn A, Herzka DA, Lederman RJ, Kocaturk O. A 20-gauge active needle design with thin-film printed circuitry for interventional MRI at 0.55T. Magn Reson Med. 2021 Sep;86(3):1786–1801. doi: 10.1002/mrm.28804. Epub 2021 Apr 16. PMID: 33860962. [PubMed: 33860962]

58. Monzel WJ, Hoff BW, Maestas SS, French DM, Hayden SC, "Dielectric breakdown of additively manufactured polymeric materials," in IEEE Transactions on Dielectrics and Electrical Insulation, vol. 22, no. 6, pp. 3543–3549, December 2015.

59. Juchem C, Nixon TW, McIntyre S, Rothman DL, de Graaf RA. Magnetic field modeling with a set of individual localized coils. J Magn Reson. 2010 Jun;204(2):281–9. doi: 10.1016/j.jmr.2010.03.008. Epub 2010 Mar 11. PMID: 20347360; PMCID: PMC2884296. [PubMed: 20347360]

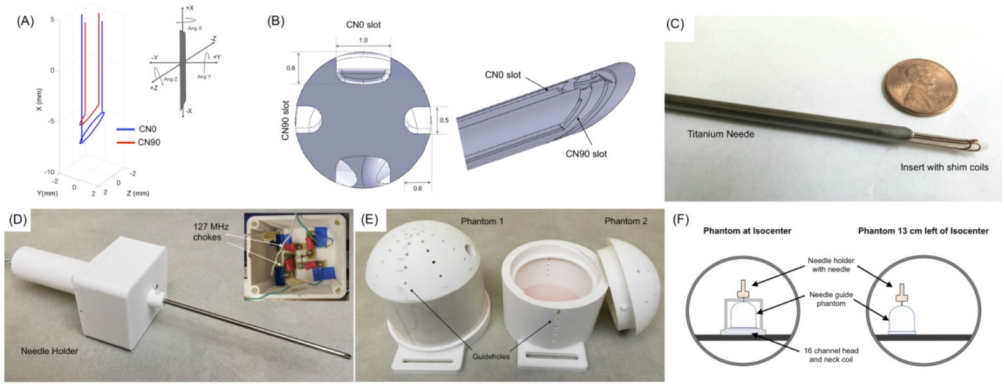

Figure 1.

Active shimming hardware (a) Selected 2 coil shim paths. CN90 (red) is a 1/2 turn angled loop and CN0 (blue) is a split tip double wire loop. The needle tip is at −10 mm along the X axis. Inset: Definition of needle orientation and rotations in the magnet frame. (b) Shim insert design with bevel and orthogonal slots for shim wires (c) Shim insert inside the titanium needle (d) Needle placed in holder with compartment for electronics and shim connections (e) 2D printed phantoms with guide holes at different angles. Phantom 1 was water-tight with no holes on the sides. Phantom 2 had a screw top for placement of samples and side insertion guide holes (f) Position of the phantom and needle for the calibration and shimming experiments. Needle is shown in the 0,0,0-degree position.

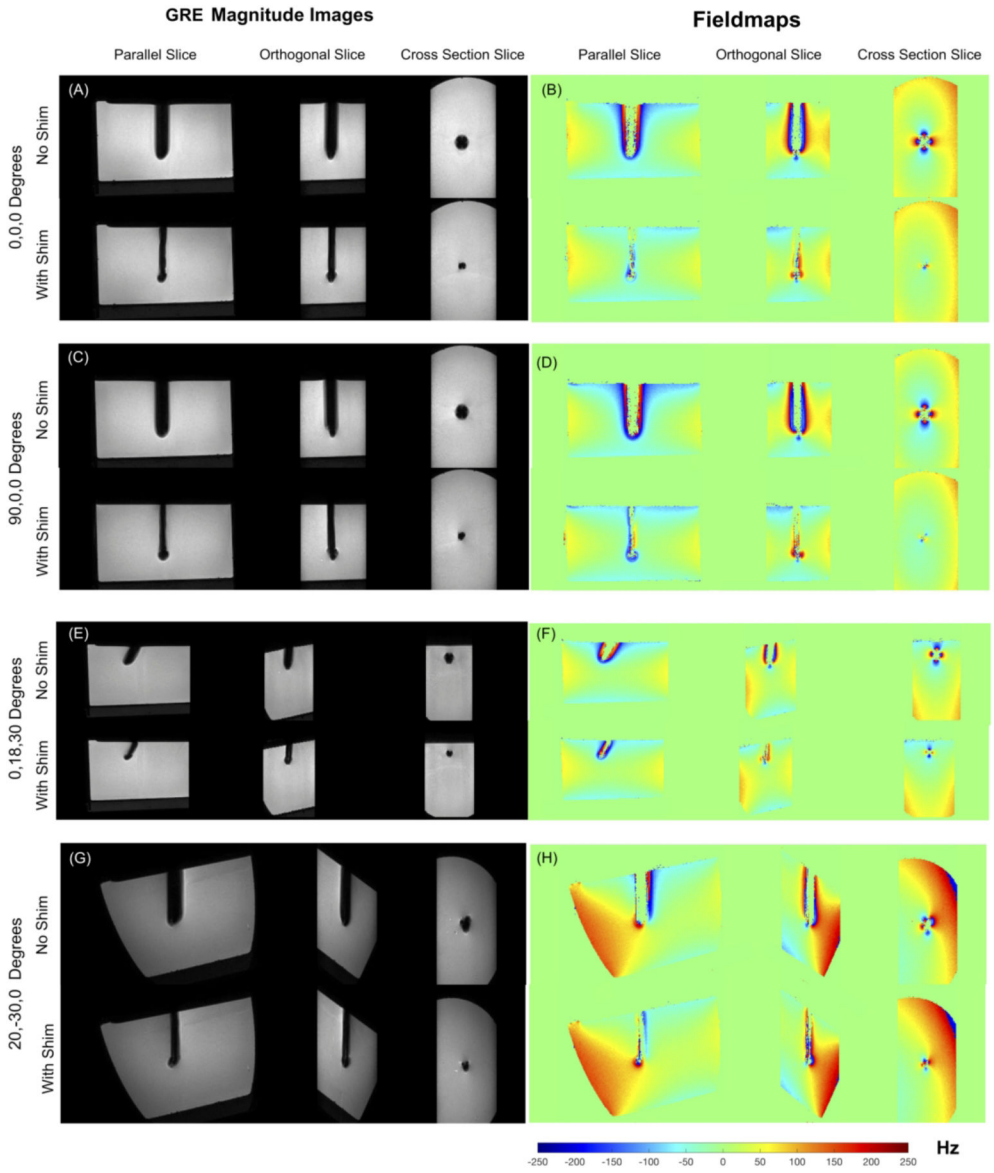

Figure 2.

Results of Needle shimming. (a-h) 1 x 1 x 1 mm^3 3D GRE images and fieldmaps showing results of active shimming. Excellent recovery of lost signal is achieved in all orientations using pre-estimated shim currents. The width of the signal void approaches the needle width in all cases. Fieldmaps show correction of the underlying ΔB_0. Without shimming, field wraps are observed closed to the needle due to extreme ΔB_0 values, which is corrected with shimming. Also, regions closest to the needle with field information in the 'Wth Shim' case have no corresponding data in the 'No Shim' case due to the signal loss.

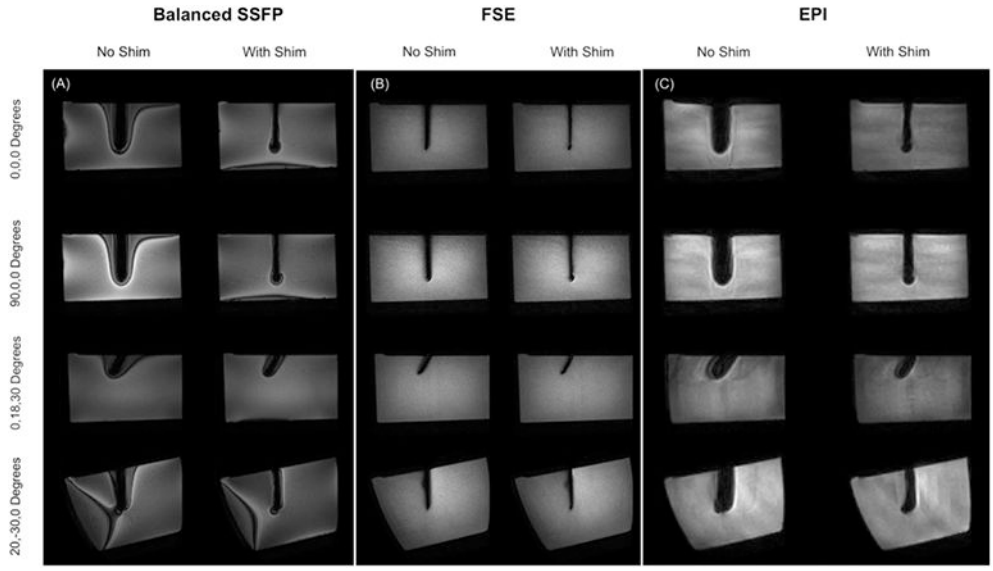

Figure 3.

Results of active shimming in 1 x 1 x 2 mm^3 Balanced SSFP, 1 x 1 x 1 mm^3 FSE and 2 x 2 x 2 mm^3 3 shot EPI images. Recovery of lost signal is achieved in all sequences and all orientations. Balanced SSFP images show reduced off-resonance related banding. The void in the FSE images approaches the true width of the 4 mm needle after shimming.

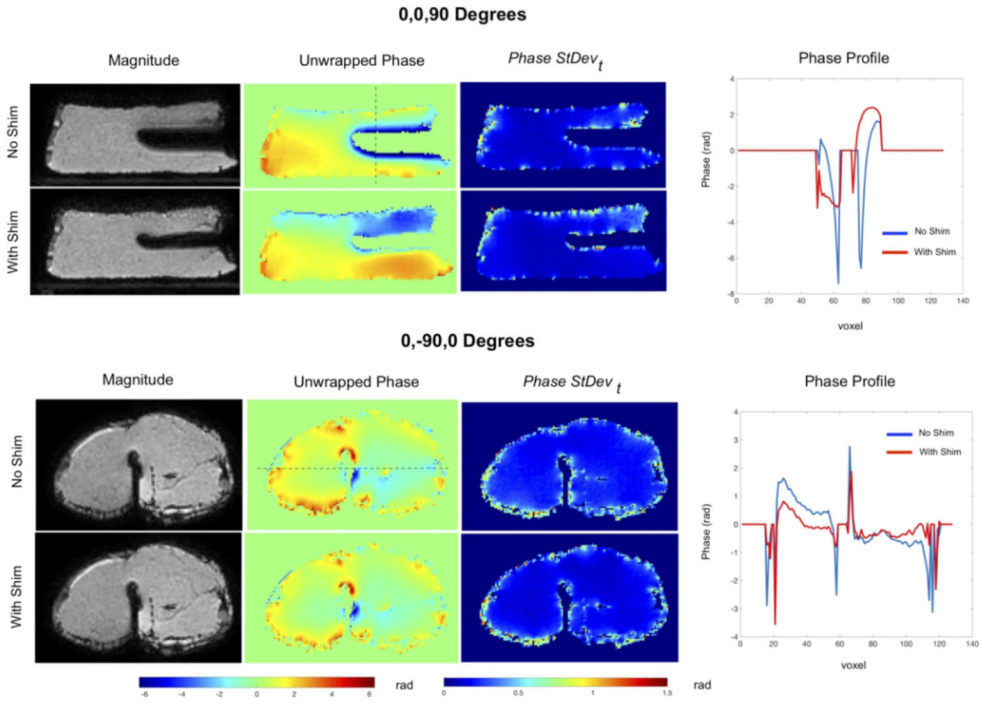

Figure 4.

Results of the *ex-vivo* porcine tissue imaging experiment. Magnitude, unwrapped phase and standard deviation maps of the phase over all time points for needle in two orientations. Also shown are profiles across the phase maps. In the perpendicular orientation (0,0 90 degrees), needle shimming reduces the signal void significantly. Also, the phase profile shows a sharp gradient in the region outside the already larger signal void without shimming, which is reduced with shimming. Shimming does not reduce the signal void noticeably when the needle is parallel to B_0 at (0,−90,0 degrees), indicating that the shim coil tip design for this insert was not optimal for parallel orientations. Slight flattening is however noticed in the underlying phase profile

Table 1

Results of heating tests of the needle shims at a position 15 cm right of isocenter in two orientations, perpendicular to B_0 (0,0,0 degrees) and parallel to B_0 (0,−90,0 degrees) (A) With shim insert inside needle (B) Only shim insert, without the needle, (C): In-scanner Reference with no needle or shim insert, (D) On the bench, outside the scanner with temperature probes directly on shim coils and the shim insert immersed vertically at the center of the phantom.

A. Temperature Rise in °Celsius With Needle (Probes on Needle Surface)

Angle	3D FSE						Continuous 2D SSFP					
	No Current		1A in CN0		1A in CN90		No Current		1 A in CN0		1 A in CN90	
	P1	P2	P1	P2	P1	P2	P1	P2	P1	P2	P1	P2
0,0,0. (Perpendicular to B_0)	1.50	0.30	1.60	0.50	1.50	0.76	0.60	0.30	0.80	0.60	0.90	0.70
0, −90,0. (Parallel to B_0)	1.90	0.90	2.79	1.47	2.00	1.00	1.17	0.51	1.40	0.79	1.34	0.63

B. Temperature Rise in °Celsius Without Needle (Probes on shim coils directly)

Position	Angle	3D FSE						Continuous 2D SSFP					
		No Current		1A in CN0		1A in CN90		No Current		1 A in CN0		1 A in CN90	
		P1	P2	P1	P2	P1	P2	P1	P2	P1	P2	P1	P2
	0,0,0. (Perpendicular to B_0)	1.67	1.74	2.34	2.60	2.20	2.49	1.63	1.29	1.9	1.46	1.76	1.60
	0, −90,0. (Parallel to B_0)	1.44	0.43	2.34	1.24	2.04	0.76	1.14	0.36	1.70	0.6	1.51	0.70

	***C. in-scanner* Reference No needle or shim Insert, No Current P1 at center, P2 at off-center position**				***D. Phantom On Bench* Reference Probes on shim coils.**			
	3D FSE		2D SSFP		1 A in CN0		1 A in CN90	
	P1	P2	P1	P2	P1	P2	P1	P2
	0.20	1.11	0.20	0.39	0.21	0.23	0.27	0.40